




ARTICLE

<https://doi.org/10.1038/s41467-020-14426-6>

OPEN

Synchronously wired infrared antennas for resonant single-quantum-well photodetection up to room temperature

Hideki T. Miyazaki ^{1*}, Takaaki Mano ¹, Takeshi Kasaya¹, Hirotaka Osato ¹, Kazuhiro Watanabe¹, Yoshimasa Sugimoto¹, Takuya Kawazu¹, Yukinaga Arai¹, Akitsu Shigetou¹, Tetsuyuki Ochiai¹, Yoji Jimba² & Hiroshi Miyazaki³

Optical patch antennas sandwiching dielectrics between metal layers have been used as deep subwavelength building blocks of metasurfaces for perfect absorbers and thermal emitters. However, for applications of these metasurfaces for optoelectronic devices, wiring to each electrically isolated antenna is indispensable for biasing and current flow. Here we show that geometrically engineered metallic wires interconnecting the antennas can function to synchronize the optical phases for promoting coherent resonance, not only as electrical conductors. Antennas connected with optimally folded wires are applied to intersubband infrared photodetectors with a single 4-nm-thick quantum well, and a polarization-independent external quantum efficiency as high as 61% (responsivity 3.3 A W^{-1} , peak wavelength $6.7 \mu\text{m}$) at 78 K, even extending to room temperature, is demonstrated. Applications of synchronously wired antennas are not limited to photodetectors, but are expected to serve as a fundamental architecture of arrayed subwavelength resonators for optoelectronic devices such as emitters and modulators.

¹ National Institute for Materials Science, Tsukuba, Ibaraki 305-0047, Japan. ² Nihon University, Koriyama, Fukushima 963-8642, Japan. ³ Tohoku University, Sendai, Miyagi 980-8579, Japan. *email: MIYAZAKI.Hideki@nims.go.jp

The manipulation of electromagnetic waves with arrayed subwavelength resonators has long been a major topic in electronic engineering. Yagi–Uda antennas generate sharp beams from a half-wave emitter through near-field mutual coupling with parasitic elements arranged with deep subwavelength spacing^{1,2}. They present the most classic yet the most advanced form of coupled subwavelength resonators, and have extended the application range to the visible region³. Phase-gradient metasurfaces, which create arbitrary wavefronts using arrays of deep subwavelength antennas with unequal shapes, have given rise to a new frontier in metamaterials that had previously focused on three-dimensional bulk materials⁴. In these metasurfaces, the spacing between the antennas is smaller than the wavelength, but not too small to avoid strong near-field mutual coupling. Recently, through far-field mutual coupling, deep subwavelength resonators arranged with optimized wavelength-sized distances have demonstrated a coherent laser oscillation equivalent to a single, large, and high-power surface-emitting laser⁵.

Arrays of optical patch antennas⁶ have also been used for perfect absorbers⁷ and thermal emitters^{8,9}. Optical patch antennas are subwavelength metal–insulator–metal (MIM) cavities that exhibit the half-wave resonance of the transverse-magnetic (TM) gap plasmon mode¹⁰. One significant potential benefit of an MIM cavity is that the upper and lower metal layers can also be used as electrodes. By sandwiching functional materials, strong interaction with densely confined electromagnetic fields could enable the realization of high-performance optoelectronic devices. To achieve this, individual patch antennas electrically isolated so far should be interconnected by conducting wires. Recently, patch antennas one-dimensionally (1D) linked by simple straight wires have remarkably enhanced the sensitivity of infrared detectors¹¹, and even demonstrated gigahertz response at room temperature¹². However, their polarization dependence distorted by the wiring revealed the lack of reasonable design principles for electrical connection of arrayed patch antennas, in contrast to the extensively investigated single dipole antennas^{13,14}.

Herein, we propose a clear-cut architecture, synchronously wired antennas (SWAs), which are deep subwavelength arrayed resonators interconnected with geometrically engineered wires. We shed light on the optical functions of conducting wires between antennas. Metallic wires folded to provide optimum optical phase delay electrically connect (short-circuit) the patch antennas, without disrupting the optimized antenna resonance. In this Article, we not only clarify the physical foundations underlying the SWAs, but also present their application to mid-infrared photodetectors incorporating only a single quantum well (QW). Practical responsivity without polarization dependence at a predetermined wavelength in the fingerprint region, extending up to room temperature, is promising for spectroscopic applications^{15–18} and free-space data transfer¹². However, applications are not limited to detectors; SWAs offer greater design freedom as a fundamental platform for optoelectronic metadevices^{19–21}.

Results

Connecting antennas by conducting wires. We discuss optical patch antennas sandwiching GaAs/AlGaAs QW infrared photodetectors (QWIPs)^{22,23} with the sensitivity peak at $\lambda = 6.7 \mu\text{m}$ between two Au layers. QWIPs absorb infrared light based on intersubband transitions (ISBT) and generate a photoconductive current by applying a bias voltage. The peak wavelength can be selected artificially by the QW design. However, QWIPs have two shortcomings. First, because of the ISBT selection rule, QWIPs can absorb only the vertical component of electric field relative to the QWs (E_z)²⁴. Thus, there is no sensitivity to normal incidence, and techniques such as oblique incidence and diffraction gratings

are required. Another drawback is the low absorption of ISBT compared to the interband transition. Both of these problems can be overcome by incorporating QWIPs into optical patch antennas. Patch antennas rotate the horizontal electric field, E_x , of normal incidence to a vertical field, E_z , through magnetic coupling (H_y). Furthermore, the magnitude of E_z is resonantly enhanced by the confinement of the field to a small volume. Both effects essentially magnify the sensitivity^{11,12,25}.

First, based on a numerical model study, we observe how the properties of arrayed optical antennas are manipulated by wiring. The thickness of the QWIP (semiconductor) layer, its effective index, and the thicknesses of the upper and lower Au layers herein are $T = 200 \text{ nm}$, $3.05 + 0.03i$, 100 nm , and 200 nm , respectively. These correspond to the experimental parameters that will be presented later.

An array of square antennas with a side length $L = 1.08 \mu\text{m}$ ($\lambda/6.2$) and period $P = 2.0 \mu\text{m}$ ($\lambda/3.4$) exhibits nearly perfect absorption at the QW sensitivity peak, irrespective of the polarization (Fig. 1a, right). Each antenna supports a half-wave resonance of E_z (Fig. 1a, center). E_z at both edges in the x -direction exhibits maximum amplitude but with the opposite polarity. The crucial requirements for a photodetector are maximizing the photocurrent (i.e., optical area) while minimizing the dark current (i.e., electrical area)^{11,12,26}. The latter is particularly important for high temperatures, where the dark current dominates. Although the optical area can exceed the geometrical size of the antenna (up to $\sim P^2$)^{27–29}, the electrical area is simply the geometrical size of the semiconductor layer. In the arrayed antennas discussed here (Fig. 1a, left), the semiconductor layer outside the Au patches is completely removed for minimizing the electrical area. Nevertheless, the resultant structure does not function as a detector, because there is no way for collecting the photocurrent. The most straightforward way to realize biasing and current extraction while minimizing the electrical area would be by connecting the patch antennas with thin wires (Fig. 1b, left). However, if linear wires with a width of $W = 100 \text{ nm}$ are added between the antennas, the electric field at the QW sensitivity peak reduces drastically (Fig. 1b, center). Because the resonator edges with opposite polarities are short-circuited by the conductive wires, the deterioration of resonance might seem to be natural. However, the resonance is not diminished, but is moved to another center frequency, even gaining a higher quality factor (Fig. 1b, right). This suggests that the wires are performing substantial functions as plasmonic waveguides. Here, we found that the original resonance can be restored by folding the wires to form a Z shape (crank shape) and adjusting their lengths, without enlarging the electrical area (Fig. 1c). Many similar solutions can be found; e.g., S-shaped wires but with different total lengths (Fig. 1d).

Demonstration of antenna-enhanced infrared photodetectors.

Optical patch antennas sandwiching QWIP layers, interconnected by folded wires, were fabricated and characterized. In addition to the SWAs, we incorporated two other important factors—a single QW and built-in ohmic contacts³⁰.

The responsivity, R , of a QWIP is proportional to the absorption efficiency (internal quantum efficiency), η_{abs} , and the photoconductive gain, g ; $R = e/(h\nu) \times \eta_{\text{abs}} \times g = e/(h\nu) \times \eta_{\text{conv}}$, where e is the electron charge, h is Planck's constant, ν is the frequency, and $\eta_{\text{conv}} = g \eta_{\text{abs}}$ is the conversion efficiency (external quantum efficiency). Here, the terminology of Schneider and Liu²³ is followed. In a conventional QWIP, R is independent of the number of QWs, N_{qw} , because $\eta_{\text{abs}} \propto N_{\text{qw}}$, but $g \propto 1/N_{\text{qw}}$. However, the detectivity that defines the signal-to-noise ratio (SNR) is higher for larger N_{qw} ; thus, N_{qw} in the order of 10 has been preferred conventionally. Nevertheless, in a

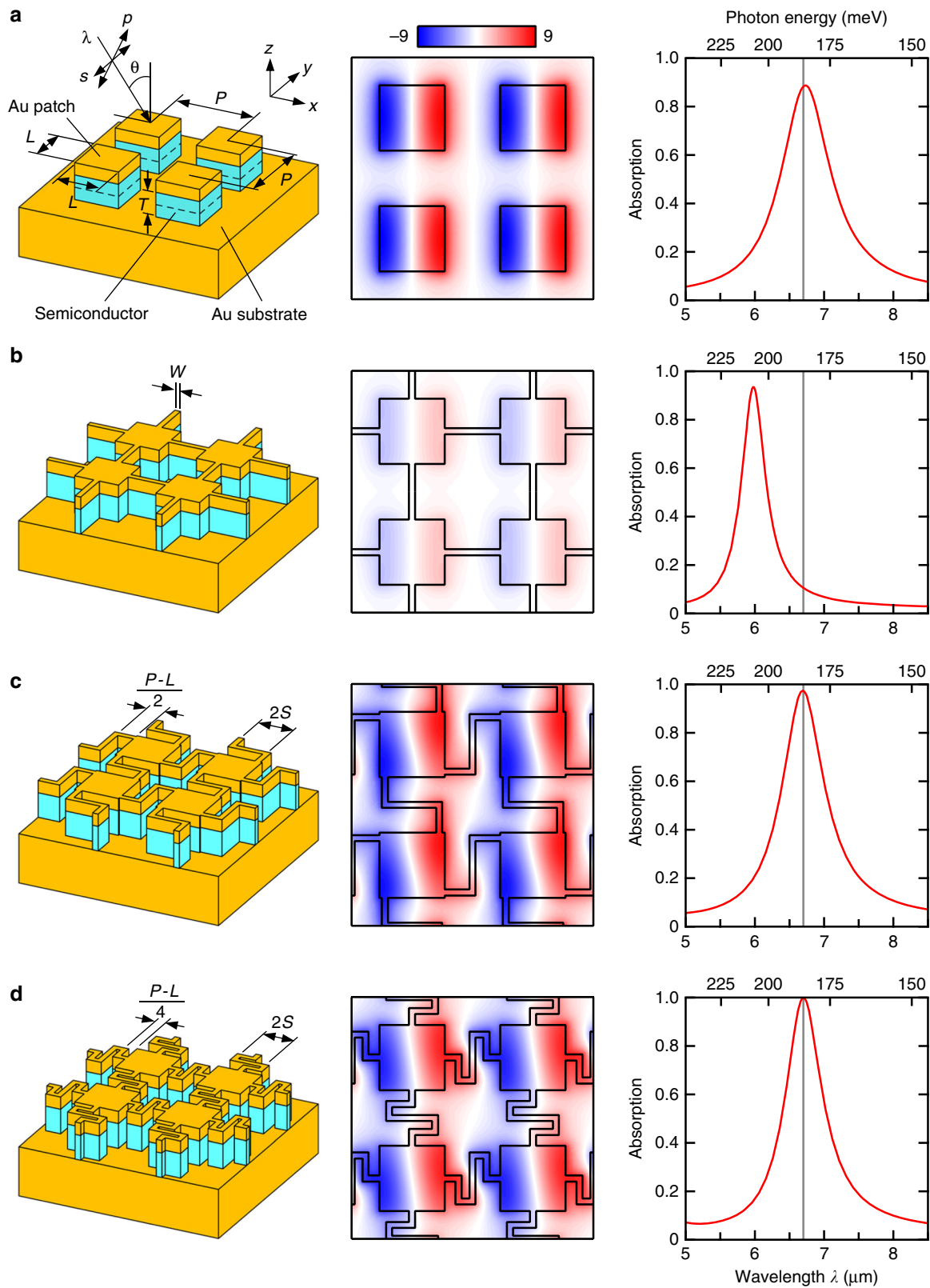


Fig. 1 Structure (left), E_z distribution at $\lambda = 6.7 \mu\text{m}$ (center) and absorption spectra (right) of the arrayed optical patch antennas. **a** Array of isolated antennas serving as the fundamental structure for this model study. **b–d** Antennas connected with **b** straight, **c** Z-shaped ($S = 0.45 \mu\text{m}$) and **d** S-shaped ($S = 0.38 \mu\text{m}$) wires. The schematics show the definitions of the coordinate system, incidence angle, polarization, and dimensions. $L = 1.08 \mu\text{m}$, $P = 2.0 \mu\text{m}$, $T = 200 \text{ nm}$, and $W = 100 \text{ nm}$. The vertical lines in the absorption spectra represent the sensitivity peak wavelength of QW ($\lambda = 6.7 \mu\text{m}$). The center column shows the snapshots of E_z at its maximum moment on the center xy plane of the semiconductor layer (broken lines in the schematic of **a**) for x polarization, $\theta = 0^\circ$; the value is normalized by the incident electric field.

QWIP with vastly enhanced absorption by the cavities, R is inversely proportional to N_{qw} because η_{abs} no longer depends on N_{qw} ^{11,12,23,29}. The dark-current-limited detectivity is also higher for smaller N_{qw} . Therefore, we employed a single QW ($N_{\text{qw}} = 1$), which also leads to a higher field enhancement because of a thinner semiconductor layer.

Among the III–V semiconductor materials used for QWIPs, GaAs/AlGaAs is a well-established system. However, there is a drawback with GaAs regarding its electrical connection with a metal, i.e., alloying is necessary for a low-resistance ohmic contact. Alloyed interlayers are unacceptable for plasmonic devices that require smooth, abrupt, controlled metal–semiconductor interfaces. We realized the double-sided nonalloyed ohmic contacts to GaAs by optimizing the dopant density and growth temperature³⁰. The ohmic contact to the originally buried surface particularly required the precise tuning of growth conditions. Now the low-resistance structure is epitaxially built-in; therefore, both the metal–semiconductor interfaces satisfy both electric and plasmonic requirements only by depositing metals.

The QW was designed based on the standard bound-to-continuum structure²². The details of design, fabrication, and characterization of the specimens are given in Methods. The temperature of the detector is 78 K, unless specified otherwise. The QWIP layer ($T = 200$ nm) was made of a 4-nm-thick GaAs QW sandwiched by 50-nm $\text{Al}_{0.3}\text{Ga}_{0.7}\text{As}$ barrier layers and 48-nm GaAs built-in ohmic contact layers (Fig. 2a). The quantum structures were fabricated by molecular beam epitaxy on n-GaAs substrates. Before incorporating into SWA structures, we fabricated a Brewster-angle incidence detector as a reference detector, to confirm the intrinsic properties of the QWIP layer. A peak unpolarized responsivity of $R_p = 4.1 \text{ mA W}^{-1}$ at $6.73 \mu\text{m}$ (Fig. 2d, top), consistent with the design, was obtained.

The wafer transfer technique is indispensable to the incorporation of epitaxial semiconductor layer into the optical patch antennas^{31–33}. The QWIP layer was transferred to another GaAs substrate through Au–Au diffusion bonding, and was sandwiched between Au layers by patterning Au/Ti SWA structures on the top using electron-beam drawing. Finally, the GaAs/AlGaAs layers other than the antennas and wires were removed by vertical dry etching, to minimize the electrical area. To investigate the effects of wire geometries on the photodetector performances systematically, SWAs with various wire folding shapes and lengths, S , were fabricated. Representative wire geometries are shown in Fig. 2b, c, and Supplementary Fig. 1b (see also Supplementary Note 1).

The absorption and normal-incidence responsivity spectra of Z-shaped SWA detectors with several different S values are shown in Fig. 2d (middle and bottom; note that $S = 0$ corresponds to straight wires). The results for $L = 1.19 \mu\text{m}$ rather than $1.08 \mu\text{m}$ discussed in Fig. 1 are shown because higher responsivities and detectivities were obtained despite the increased dark currents; suggesting a fair balance of the optical and electrical areas. However, the systematic dependence on S values is identical irrespective of L values.

Because the experimental absorption spectra (solid lines) could only be obtained for oblique incidence by reflection measurement, the numerical absorption spectra for $\theta = 0^\circ$ are presented for reference (broken lines). In this calculation, the semiconductor layer was exactly treated as a multilayer made of a QW, two barrier, and two contact layers, considering the free-carrier absorption and uniaxial ISBT absorption. In both absorption spectra, the peak systematically moves to the longer side for a larger S . The responsivity peak wavelengths elongate simultaneously within the sensitivity range of the Brewster-angle detector ($3\text{--}8 \mu\text{m}$). When the absorption peak of the

SWAs for $\theta = 0^\circ$ (Fig. 2d, middle, broken lines) and the responsivity peaks of the QWIP layer (Fig. 2d, top) coincide ($S = 0.29 \mu\text{m}$), the maximum responsivity $R_p = 3.3 \text{ A W}^{-1}$ ($\eta_{\text{conv}} = 0.61$) was recorded at $6.67 \mu\text{m}$ (Fig. 2d, bottom). The responsivity was enhanced by a factor of 803 compared with that of the Brewster-angle reference detector. To estimate the theoretical responsivity from the numerical absorption, the value of g is necessary. The spectral density of the dark-current noise³⁴ gave $g = 2.3$ (Supplementary Fig. 2a), which yields good agreement between the theoretical and experimental responsivities (Supplementary Fig. 1e). The detectivities determined from dark-current and background (298 K) noises are 5.2×10^{10} and $3.9 \times 10^{10} \text{ cm Hz}^{1/2} \text{ W}^{-1}$, respectively. Thus, our detector is in a background-limited regime at 78 K. The noise-equivalent power (background incidence) is $0.26 \text{ pW Hz}^{-1/2}$.

There is no polarization dependence (Fig. 2e) due to the symmetry of SWAs. The angular dependence of η_{conv} reveals that the field of view (FOV) of the detector is relatively narrow (57° and 68° for p and s polarizations, respectively; Fig. 2f and Supplementary Fig. 1g) compared with that of the conventional unstructured detectors (120° in principle). This is because the dispersive nature of the wiring (discussed later) limits the overlapping of sensitivity range of the QW and the antenna resonance. An intrinsically small FOV is advantageous for an infrared detector in that it suppresses the photocurrent due to background radiation from unwanted directions.

The bias voltage, V_b , dependence of R_p measured using a 500°C blackbody²² at various detector temperatures is shown in Fig. 3a. The R_p is not linear with V_b , but quickly increases after an offset and exhibits a peak at a certain value, which is consistent with previous reports for $N_{\text{qw}} = 1$ ^{35,36}. The responsivity was observed up to room temperature ($R_p = 24 \text{ mA W}^{-1}$ at $V_b = +0.5 \text{ V}$, 293 K), and the peak wavelength exhibited a small red shift for a higher temperature (Fig. 3b). The background-limited performance (BLIP) temperature, specifying the operation range of a photon detector uninfluenced by the dark current, was 87 K (Supplementary Fig. 2c).

Previously, room-temperature sensitivity of photoconductive QWIPs had been observed only for intense laser sources³⁷. Recent antenna-enhanced QWIPs¹² with $N_{\text{qw}} = 5$ demonstrated the first room-temperature response for a blackbody emitter at 1000°C , in addition to $\eta_{\text{conv}} = 12.4\%$ ($R_p = 0.9 \text{ A W}^{-1}$ at $\lambda = 9 \mu\text{m}$) and background-limited detectivity of $1.5 \times 10^{10} \text{ cm Hz}^{1/2} \text{ W}^{-1}$ at 78 K. In the present work, using polarization-independent SWAs and $N_{\text{qw}} = 1$ realized higher performances (61% and $3.9 \times 10^{10} \text{ cm Hz}^{1/2} \text{ W}^{-1}$ at 78 K), and room-temperature sensitivity for a blackbody at a lower temperature (500°C). Although a straightforward comparison is difficult because of the difference in the peak wavelengths and FOVs for background measurement, our SWA-enhanced QWIP is one of the best GaAs-based mid-infrared photodetectors. This was achieved by enhancing the weak response of a single QW with SWAs (see Supplementary Fig. 3 and Supplementary Note 2 for detailed discussion).

Resonance engineering based on wire geometry. As has been shown, numerical simulation offers accurate optical properties of SWAs with arbitrary wire geometry, but does not explain why the folding shape and lengths of wires control the resonance of SWAs. Through simple models, here we clarify the optical functions of the wires. Only the key findings are presented here, while the detailed calculation method and discussions are presented in Methods and Supplementary Notes 3 and 4.

Resonance is excited by the coupling of incident light with the in-plane propagation modes. For simplicity, the discussion is restricted to propagation in the x -direction by the p -polarized

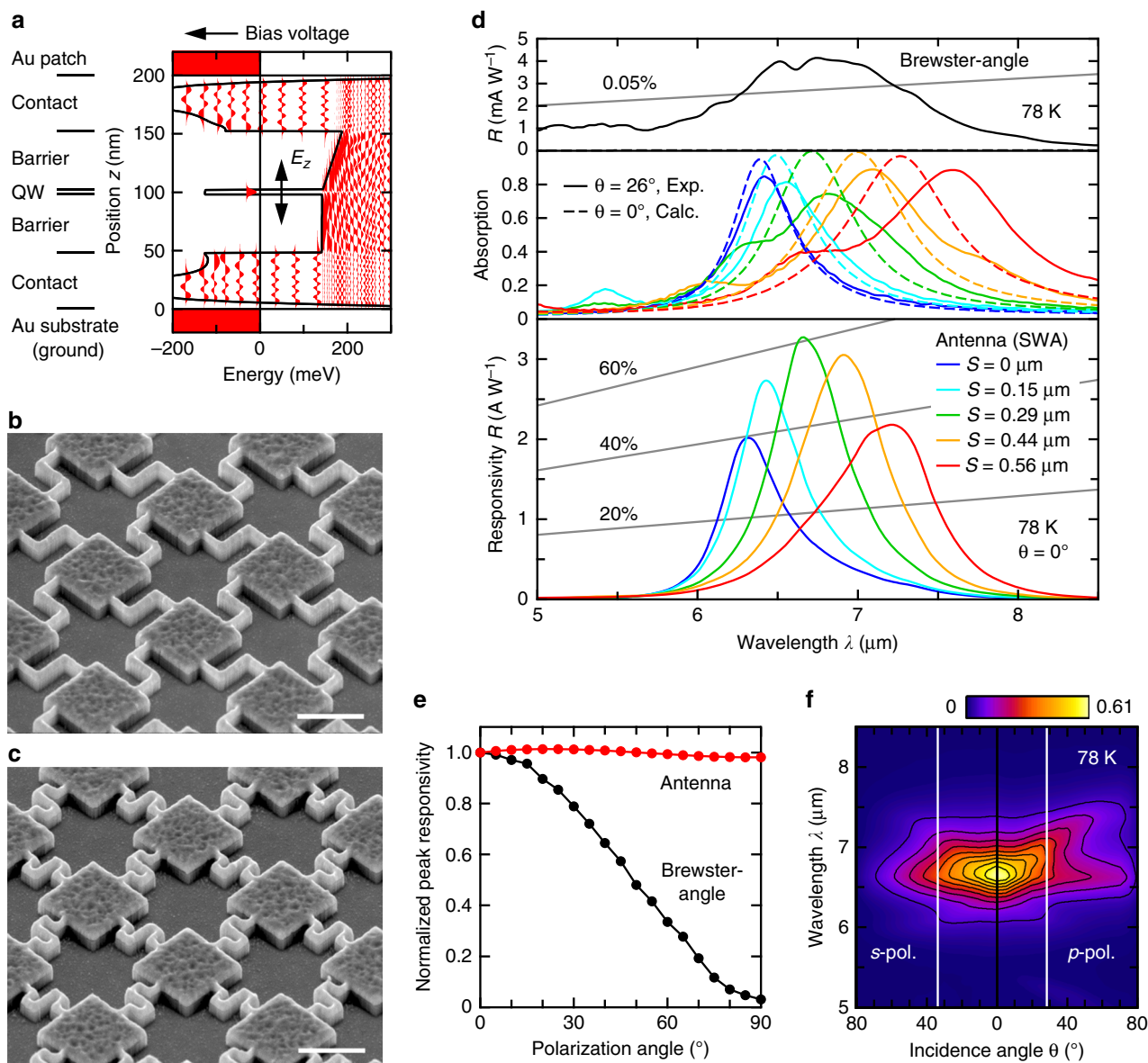


Fig. 2 Fabrication and characterization of wired-antenna-enhanced QWIPs. **a** QW design, and numerical conduction band profile and wave functions based on experimental dopant density distribution. **b** Scanning electron micrograph of SWAs with Z-shaped ($S = 0.29 \mu\text{m}$) and **c** S-shaped ($S = 0.22 \mu\text{m}$) wires. Bar: $1 \mu\text{m}$. **d** Responsivity spectrum of the reference Brewster-angle detector (top), absorption spectra for Z-shaped SWAs with various S values measured for $\theta = 26^\circ$, s-polarized incidence (solid lines, middle) and calculated for $\theta = 0^\circ$ (broken lines, middle), and the corresponding responsivity spectra for $\theta = 0^\circ$ (bottom). Equiefficiency (η_{conv}) lines are also plotted. **e, f** Other properties for the detector with the maximum responsivity (Z-shaped, $S = 0.29 \mu\text{m}$). **e** Polarization angle dependence of R_p . Results for the Brewster-angle detector are also shown for reference. **f** Incidence-angle dependence of η_{conv} for p- (right) and s-polarization (left). Vertical lines denote the FOV/2 at half height.

incidence in the xz plane, which excites the TM modes. In-plane wave vector in SWAs, k_x , is discussed.

The numerically obtained k_x dependence of the absorption spectra of SWAs corresponding to Fig. 1a–d is shown in Fig. 4a–d as color maps, respectively. The resonance wavelengths for normal incidence ($\theta = 0^\circ$) presented in Fig. 1 appear as peaks at $k_x = 0$ (red arrows). The array of isolated antennas exhibits a flat mode (Fig. 4a); however, it is fundamentally modified when wired. Marked angular dispersion arises and the resonance wavelength changes, both of which greatly depend on the folding shape and length of wires (Fig. 4b–d). Our aim here is to reproduce these angular dispersions by a simple, insightful model.

Most features can be explained by the propagation properties of individual building blocks—antennas and wires. Numerically

obtained wave vectors, k_{antenna} and k_{wire} , of the TM-like plasmon mode of an infinitely long MIM waveguide of width L and infinitely repeated units of folded wires with a length, $P-L$, are shown in Fig. 4e, f, respectively, in an extended zone scheme.

An MIM waveguide of width L (Fig. 4e) supports a propagating mode close to the infinitely wide waveguide^{38,39}. A square patch antenna of side length L is an MIM waveguide of width L terminated at a length L . Its resonance wavelength is given by

$$\text{Re}(k_{\text{antenna}}) \times L = \pi, \tag{1}$$

where Re denotes the real part. Because the resonance is localized at each antenna, the same condition holds true for the resonance of arrayed isolated antennas. The dispersion deduced from Eq. (1) is superimposed with a broken line in Fig. 4a. Both the

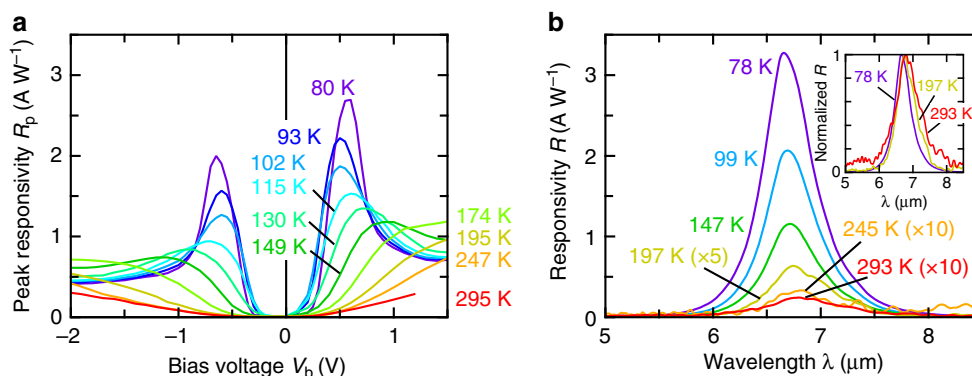


Fig. 3 Temperature dependence of the responsivity of wired-antenna-enhanced QWIPs. Z-shaped, $S = 0.29 \mu\text{m}$. **a** Bias dependence of R_p at various detector temperatures, measured with a blackbody at 500°C . **b** Temperature dependence of spectroscopic responsivity at their respective peak bias voltages. For 197 K, 245 K, and 293 K, the spectra were obtained at $V_b = +0.5 \text{ V}$, as no peak could be specified. The inset shows the normalized spectra at representative temperatures including the one at room temperature (293 K).

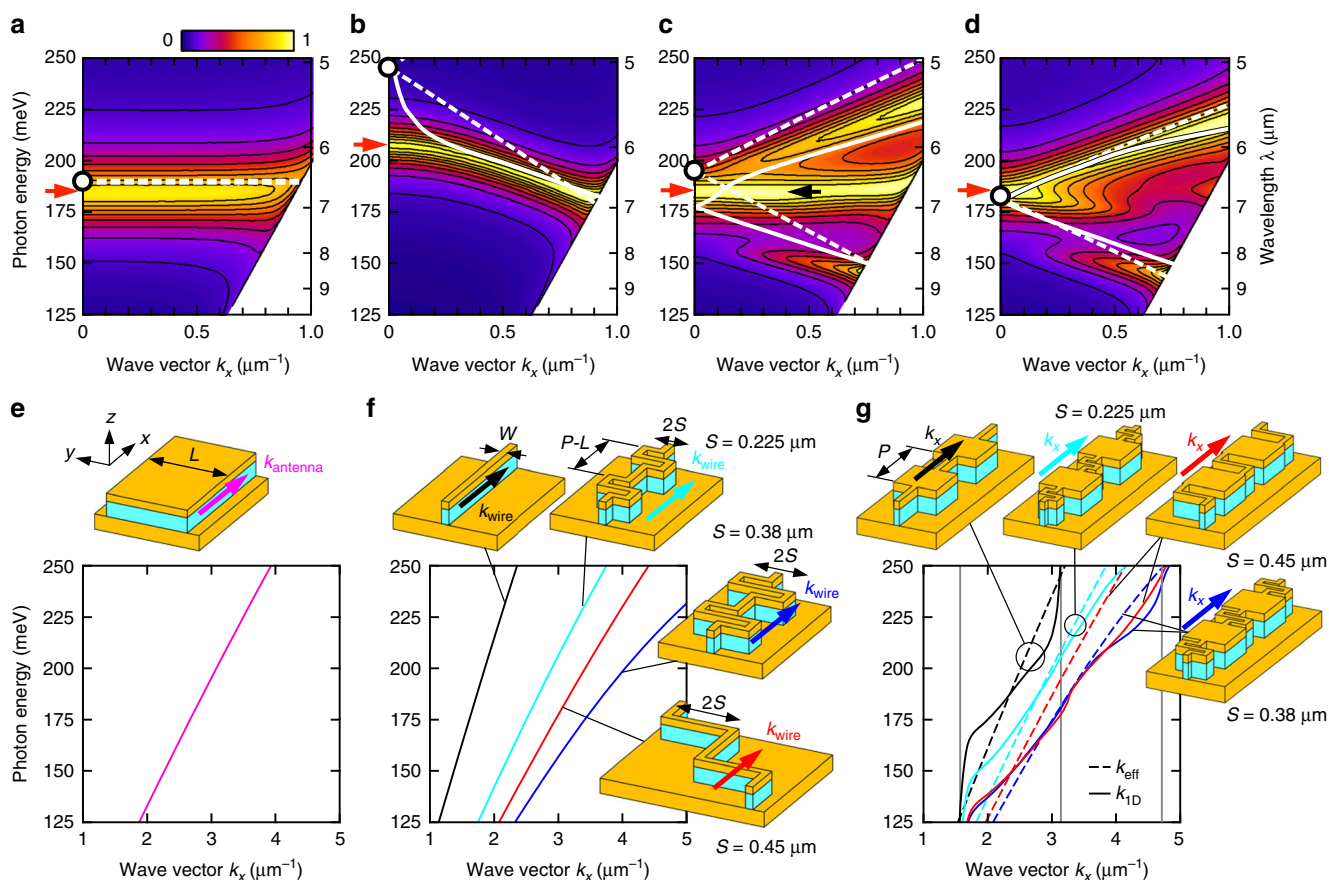


Fig. 4 Resonance engineering of arrayed antennas based on wire geometry. **a–d** Wave-vector dependence of absorption spectra for p -polarized incidence. **a** Array of isolated antennas. **b** Antennas connected with straight, **c** Z-shaped ($S = 0.45 \mu\text{m}$), and **d** S-shaped ($S = 0.38 \mu\text{m}$) wires. **e–g** Dispersion relation (real part) of TM-like propagation mode in elementary structures illustrated by the schematics. **e** MIM waveguide with width L . This dispersion gives the resonance of arrayed isolated antennas represented in **a** by a broken line. **f** Infinitely repeated folded plasmonic wires. **g** 1D periodic system made of antennas and wires, k_{1D} (solid curves). The broken lines are k_{eff} based on Eq. (2). The dispersions of wired antennas represented by solid and broken lines in **g** are also displayed by solid and broken lines in **b–d**. The vertical gray lines denote the BZ edges where bandgaps can appear.

resonance wavelength (circle) and wave-vector dependence are well described herein.

The dispersion of wires (Fig. 4f, see definition in “Methods” section) varies in a wide range depending on the geometry; this variety gives the foundation of the high degree of design freedom

of SWAs. The value of k_{wire} at a fixed photon energy (wavelength) depends both on the physical length of the wire and the folding shape. The former is natural because the phase rotates more while traveling unit length $P-L$ in the x direction. Besides, the speed of the propagating plasmon wave varies depending on its location

along the wires, particularly around the winding parts in the S-shaped wires (Supplementary Figs. 4 and 5). As a consequence, the accumulated phase rotation spanning unit length $P-L$ in the x -direction depends on the folding shape. As expected, intermediate-shaped wires yield intermediate properties (Supplementary Note 5 and Supplementary Fig. 6).

The effective wave vector of a combined system of wires and antennas can be given by

$$k_{\text{eff}} = k_{\text{antenna}} \times L/P + k_{\text{wire}} \times (P - L)/P, \quad (2)$$

where the phase jump at the wire–antenna interface was ignored. Because k_{wire} is included here, the wired antennas exhibit a resonance wavelength essentially different from that of the arrayed isolated antennas. In Fig. 4g, k_{eff} is represented by broken lines. In Fig. 4b–d, the same results are shown by white broken lines in a reduced zone scheme. The resonance wavelengths for $\theta = 0^\circ$ are given by $\text{Re}(k_{\text{eff}}) \times P = 2\pi$ and denoted by circles. This simple model gives a sound description of the rigorous results in Fig. 4c, d.

However, the result for straight wires in Fig. 4b needs a more accurate model. We discuss a 1D array of wires and antennas, where the mismatch at the wire–antenna interface is considered. The obtained wave vectors, k_{1D} (see definition in “Methods” section) are represented in Fig. 4g by solid lines. k_{1D} deviates from k_{eff} near the Brillouin zone (BZ) edges (vertical lines). This implies the formation of bandgaps by reflection, i.e., impedance mismatch, at the wire–antenna boundaries (the bandgap is blurred by absorption. See Supplementary Note 4 for remarks). The white solid lines in Fig. 4b–d represent k_{1D} in a reduced zone scheme. This time, the model describes the rigorous result for the straight wire (Fig. 4b) for the most part (except for the vertical tail due to the bandgap). The discussion thus far would be sufficient to understand that the plasmonic propagation through the wires determines the resonance of SWAs.

In summary, (i) the conducting wires provide optical phase delay between the antennas depending on the folding shapes and dimensions, and (ii) the reflection at the wire–antenna interface also influences the overall properties of SWAs.

The residual discrepancies, e.g., the horizontal mode denoted by a black arrow in Fig. 4c, originate from the coupling in the y -direction (see Supplementary Movie 1 and Supplementary Note 4).

Discussion

In summary, we demonstrated that an overlooked factor—the geometry of wires—functions as a new design freedom for tuning the resonance wavelength of arrayed antennas while minimizing their electrical areas, and enhances the infrared responsivity of QWIPs. Optical patch antennas sandwiching a QWIP interconnected with folded wires achieved a polarization-independent conversion efficiency exceeding 60% and room-temperature sensitivity for a 500 °C blackbody, when the absorption wavelength of the QW and the resonance wavelength of the wired antennas agree with each other.

Despite these excellent properties, the detectors have not been optimized fully yet. Antenna designs balancing the optical and electrical areas should be thoroughly investigated. The layer configuration of the QWIPs also needs improvement to maximize the ISBT absorption. QWIPs made of other materials (e.g., InGaAs/InP)⁴⁰ have shown similar or higher responsivity and detectivity; SWAs can be combined with these materials as well. Through these optimizations, less toxic SWA-enhanced QWIPs would replace the widely used but toxic HgCdTe detectors²⁶ in some spectroscopic applications^{15–18}. As Palaferri et al. demonstrated¹², gigahertz-frequency detection would be another

promising application that only antenna-enhanced QWIPs can realize.

We stress here that all the structures, both the quantum nanostructures manipulating the electron wave functions and the antennas controlling the electromagnetic waves, were artificially created and yielded quantitatively reasonable properties (see Supplementary Notes 6 and 7). Such highly engineered structures suggest a novel and important frontier in optoelectronics. SWAs can also be applied to various semiconductor structures other than QWIPs to realize thin photodetectors with high absorption ideal for reducing dark currents^{26,41}. Moreover, SWAs are expected to serve as a fundamental architecture of arrayed subwavelength resonators for optoelectronic metadevices such as solar cells, emitters, and modulators^{19–21}.

SWA and three other types of arrayed subwavelength resonator introduced at the beginning are compared in Supplementary Note 8 and Supplementary Fig. 7. In a conventional array, the resonators are mutually coupled through propagation in free space, making the coupling straightforwardly dependent on the relative positions of the resonators. By contrast, in SWAs, the phase relationships can be varied widely by controlling the wire folding geometry independent of the relative antenna positions. This gives us greater freedom when designing metasurface optoelectronic devices.

Before finishing, we remark that each antenna or wire in SWAs does not have to be identical. By changing the wires and/or antennas gradually, the wavefront engineering that has been achieved using phase-gradient metasurfaces could be expanded further with wider tunability. Supplementary Note 9 and Supplementary Fig. 8 exemplifies a design of an SWA-enhanced QWIP with a high responsivity to a specific wavefront by incorporating gradually changing wires.

Methods

Design, fabrication, and evaluation of quantum wells. The QWIP structure was grown on n-GaAs (100) substrates (Si density: $1 \times 10^{18} \text{ cm}^{-3}$) using a solid-source molecular beam epitaxy system. After the growth of a GaAs buffer layer, sacrificial (etch stop) layers of $\text{Al}_{0.9}\text{Ga}_{0.1}\text{As}$ (thickness: 900 nm, Si density: $5 \times 10^{17} \text{ cm}^{-3}$) and $\text{Al}_{0.55}\text{Ga}_{0.45}\text{As}$ (100 nm, $5 \times 10^{17} \text{ cm}^{-3}$) were grown. Then, an initial-side contact layer with a total thickness of 48 nm³⁰, consisting of a highly Si-doped GaAs layer (28 nm, $1.25 \times 10^{19} \text{ cm}^{-3}$), an n-GaAs (15 nm, $3 \times 10^{18} \text{ cm}^{-3}$), and a nondoped GaAs layer (5 nm), was grown. The main part of the QWIP is made of an $\text{Al}_{0.3}\text{Ga}_{0.7}\text{As}$ barrier (50 nm), an n-GaAs QW (4 nm, $3 \times 10^{18} \text{ cm}^{-3}$, except for the final 0.85 nm), and an $\text{Al}_{0.3}\text{Ga}_{0.7}\text{As}$ barrier (50 nm). Finally, a 48-nm-thick end-side contact layer comprising an n-GaAs (20 nm, $3 \times 10^{18} \text{ cm}^{-3}$) and a highly Si-doped GaAs layer (28 nm, $1.25 \times 10^{19} \text{ cm}^{-3}$) was grown. To form the highly Si-doped GaAs layers, the growth of n-GaAs (28 nm, $5 \times 10^{18} \text{ cm}^{-3}$) was interrupted and seven δ -doping layers of Si ($3 \times 10^{12} \text{ cm}^{-2}$) with a period of 4 nm were inserted. The layers from the initial-side contact to the end-side contact conform the QWIP layer with a total thickness of $T = 200$ nm. For this QWIP layer, the growth temperature was kept at relatively low 530 °C, which is important for realizing nonalloyed ohmic contact to the initial side.

The designs of the QW and the barriers are based on the standard bound-to-continuum structure²². In the etch-stop layer, there are two layers in the Al composition. The first $\text{Al}_{0.9}\text{Ga}_{0.1}\text{As}$ layer is for high etching selectivity against the GaAs substrate and the next $\text{Al}_{0.55}\text{Ga}_{0.45}\text{As}$ finishing layer is for realizing a smooth, low-loss surface⁴². For responsivity evaluation by the Brewster-angle detector before the wafer transfer, the etch-stop layers are also doped.

The depth profile of the doped Si concentration was measured with secondary-ion mass spectrometry. The total active carrier sheet density was confirmed with the van der Pauw method for specimens made of only the QWs or contact layers³⁰.

The conduction band profiles, wave functions, and absorption spectra were numerically obtained by solving the Schrödinger and Poisson equations⁴³ and using Fermi's golden rule²⁴. Conduction band offset was based on ref. 44. However, a small correction was applied on the basis of systematic experiments; $\Delta E_c = 0.64 \Delta E_g$ was adopted at 78 K, where ΔE_c and ΔE_g are conduction band offset and bandgap difference, respectively.

The asymmetrical doping profile including a 5-nm-thick nondoped layer in the initial-side contact layer is employed, aiming at obtaining a symmetrical band profile after the segregation of the Si dopant. However, this attempt was not successful. Hence, the profile obtained was asymmetric, as shown in Fig. 2a. The asymmetry also appeared in the current–voltage properties in Supplementary Fig. 2.

Brewster-angle detectors were fabricated from a small piece of wafer. After evaluating the intrinsic responsivity of the QWIP layer, the wafer transfer was performed and the antenna-enhanced detectors were fabricated.

Because the QW was fabricated on a highly doped substrate, the measurement of the absorption spectrum by transmission was difficult. Therefore, the absorption spectrum was obtained from the responsivity spectrum of the Brewster-angle detector and the value of g ($= 3.0$), explained in Supplementary Note 1) obtained from the noise measurement. The absorption spectrum yielded an oscillator strength of 0.74 and a dipole matrix element of 1.5 nm.

Electromagnetic simulation and design of antennas. For the numerical simulation based on Maxwell's equations, several different methods were used. The numerical results shown in this paper were obtained by finite difference methods (COMSOL Multiphysics). In the early stage of this study, rigorous coupled-wave analysis (RSOFT, DiffractMOD) and finite-difference time-domain method (RSOFT, FullWAVE) were also used.

The dielectric function of Au was based on ref. 45. For Figs. 1 and 4 and Supplementary Figs. 4–6, and 8, where reflection and propagation of the overall structures are important rather than the accuracy of the electric field at the QW layer, the semiconductor QWIP layer was regarded as an isotropic wavelength-independent medium with a refractive index of $3.05 + 0.03i$, for simplicity. This value gives practically consistent results with the rigorous five-layer model.

For the rigorous analysis shown in Fig. 2 and Supplementary Figs. 1 and 3, and the Fresnel equations for the Brewster-angle detector, where an accurate vertical electric field at the QW layer is necessary for obtaining responsivity, the QWIP layer was treated as a wavelength-dependent five-layer multilayer. The QW was assumed as a uniaxial material with ISBT absorption in the vertical direction and free-carrier absorption in the lateral directions.

The wavelength-dependent refractive indices of the nondoped GaAs and $\text{Al}_{0.3}\text{Ga}_{0.7}\text{As}$ were based on ref. 46. To express the free-carrier absorption, a Drude term $-\omega_p^2/(\omega^2 + i\gamma\omega)$ was added, where ω_p and $1/\gamma$ are the plasma frequency and relaxation time, respectively⁴⁷, both of which are specified by the carrier density, N , and mobility, μ , respectively²⁴. The contact layer was regarded as an isotropic Drude material corresponding to experimentally obtained $N = 4.7 \times 10^{18} \text{ cm}^{-3}$ and $\mu = 1500 \text{ cm}^2 \text{ V}^{-1} \text{ s}^{-1}$. For the lateral directions of the QW layer, a Drude term corresponding to the experimental $N = 2.4 \times 10^{18} \text{ cm}^{-3}$ and $\mu = 2000 \text{ cm}^2 \text{ V}^{-1} \text{ s}^{-1}$ was considered. In the vertical direction of the QW layer, the ISBT absorption was described with a three-term Lorentzian model²⁷, considering the term $-\Omega_{pj}^2/(\omega^2 - \Omega_j^2 + i\Gamma_j\omega)$ ($j = 1, 2, \text{ and } 3$). We set $(\Omega_1, \Gamma_1, \Omega_{p1}) = (168, 30, 256)$, $(\Omega_2, \Gamma_2, \Omega_{p2}) = (236, 39, 114)$, and $(\Omega_3, \Gamma_3, \Omega_{p3}) = (279, 73, 124)$ in meV. These values were obtained initially by Fermi's golden rule²⁴ and then by making a small correction to $j = 1$, so that the values yielded consistent results with the experimental responsivity of the Brewster-angle detector.

The definitions of the geometry of SWAs are given in Fig. 1 and Supplementary Fig. 6. In the polarization dependence in Fig. 2e, the angle 0° corresponds to the p -polarization (x polarization for $\theta = 0^\circ$). Exactly, the Z-shaped wires with $S = 0.56 \mu\text{m}$ shown in Fig. 2d and Supplementary Fig. 1e have a slightly different definition, because the S value is so large that the wires do not fall within the side length L . In such situations, the geometry in Supplementary Fig. 1c with $F = 0.05 \mu\text{m}$ was used.

In Fig. 4 and Supplementary Figs. 4–6, to determine the in-plane propagation of the wires, k_{wire} and wire/antenna combinations, k_{1D} , five period structures were considered. An oscillating E_z was placed at the wire edge and excited TM-polarized in-plane propagating modes. An entrance straight wire with $W = 0.1 \mu\text{m}$ and a proper length was added at specific instances to stabilize the incident electromagnetic fields. The outer area of this model was terminated by perfect matching layers, so the model was equivalent to an infinitely repeated folded wire.

The definition of k_{wire} determined by numerical simulation needs a special remark. Here we are not discussing a plane wave propagating in a free space. Instead, we are considering a guided wave propagating through a deep subwavelength structure with a width $W = 0.1 \mu\text{m}$ ($< \lambda/60$) folded at a right angle several times over within a length of $P-L = 0.92 \mu\text{m}$ ($< \lambda/7$). The focus here is on how far the phase evolves before the guided wave arrives at the next square cavity placed at a distance of $P-L$ in the x -direction. To determine this, the same wire units with a length of $P-L$ in the x -direction were connected (see the schematics in Fig. 4f and Supplementary Fig. 6c), and the average phase rotation was numerically obtained with respect to the distance in the x direction. This is called k_{wire} .

The definition of k_{1D} is similar to k_{wire} . In the case of k_{1D} , the unit structure is made of one unit of wire with a length of $P-L$ in the x -direction and an MIM waveguide with width L and length L (see the schematics in Fig. 4g and Supplementary Fig. 6d). A TM-polarized wave is excited at the edge of the first wire and the average phase rotation with respect to the distance in the x -direction was numerically obtained.

Fabrication of Brewster-angle detectors. The intrinsic properties of the QWIP layer were evaluated by a Brewster-angle incidence detector. The Brewster-angle configuration exhibits a lower responsivity than the widely used back-illumination through a 45° facet, but its fabrication is easier. A Ti (bottom)/Au (top) electrode with a $100 \mu\text{m} \times 400 \mu\text{m}$ aperture was patterned on top of a mesa defined by a $\text{H}_2\text{SO}_4/\text{H}_2\text{O}_2/\text{H}_2\text{O}$ solution (1:8:1,000). The long rectangular shape is because the

light is incident from a very shallow angle. Due to the built-in ohmic layer, this electrode exhibits a low resistance only by depositing the metals. However, the substrate side needs alloying for the ohmic contact. An electrode made of Ni, AuGe, Ni, and Au was patterned on a wet-etched substrate surface and annealed at 420°C for 90 s. Although the exact Brewster angle is 73° , the detector was set at $\theta = 65^\circ$ in the actual experiment due to the restriction of the optical setup. This actual value was used in the calculation. The setup for the evaluation of the Brewster-angle detector is shown in Supplementary Fig. 1d. This detector has a sensitivity only for p -polarized incidence. In the polarization dependence in Fig. 2e, the angle 0° corresponds to the p -polarization. The definition of the sign of bias voltage is opposite to the antenna-enhanced detector, because the QWIP layer is upside down.

Wafer transfer. The QWIP layer was coated with 3-nm-thick Ti and 150-nm-thick Au layers and bonded with another n-GaAs substrate coated with 10-nm-thick Ti and 500-nm-thick Au layers at a pressure of 5 MPa and a temperature of 250°C for 60 min in N_2 atmosphere⁴⁸. After mechanical polishing, the original GaAs substrate was chemically etched by a citric acid (1 g ml^{-1})/ H_2O_2 solution (10:1) at 38°C ⁴⁹. By etching the etch-stop AlGaAs layers using HF, the 200-nm-thick epitaxial QWIP layer was transferred onto an Au substrate.

Fabrication of antenna-enhanced detectors. Wired antennas were fabricated on the transferred QWIP layer by electron-beam drawing and lift-off of 3-nm-thick Ti and 150-nm-thick Au top layers. Most of the QWIP layer was removed using a $\text{H}_2\text{SO}_4/\text{H}_2\text{O}_2/\text{H}_2\text{O}$ solution (1:8:1000), leaving only the minimum necessary areas around the antennas. Then, the specimen was coated with a 100-nm-thick SiO_2 film for electrical isolation. Windows of the SiO_2 layer were opened by dry etching using SF_6 around the detector areas. SF_6 was chosen because of its good selectivity against GaAs and excellent removal of SiO_2 on the vertical side wall of the upper Au layer. After patterning the electrode pads made of 3-nm-thick Ti and 150-nm-thick Au layers, so that one side can overlap with the edges of the wired-antenna areas, the QWIP layers not covered by the upper Au layers were vertically etched by inductively coupled plasma etching using Cl_2 and N_2 . The resultant Au layer after the dry etching was a $\sim 100 \text{ nm}$ in thickness. For the patterning of the structures, except for the first antennas, the laser-beam drawing method was used. Each detector is a $100 \mu\text{m}$ square and contains 2500 patch antennas. The global image of a detector is exemplified in Supplementary Fig. 1a.

For efficient systematic evaluation, seven such detectors with different parameters were integrated on a chip and assembled on an 8-pin ceramic package. Another pin is for the common ground. The signals were extracted by bonding an Au wire at the root of each Au electrode.

Measurement of optical properties. The detector was installed in a liquid- N_2 cryostat with ZnSe windows, and the responsivity spectra were measured with a Fourier transform infrared (FTIR) spectrometer (JASCO, FT/IR-6200). The current from the detector was amplified (NF, CA5350 and Keithley, 428, depending on the experiment) and fed into an external port of the FTIR. The spectral responsivity was quantified based on a calibrated HgCdTe detector. No corrections other than the detector areas were applied to the responsivity values. The incident light from the FTIR was unpolarized. When necessary, a wire-grid polarizer was placed in the light path. The ceramic package mounting the detector chip was in tight contact with a Cu block. The specimen in the cryostat was made to rotate around its vertical axis so that the incidence-angle dependence could be evaluated.

In addition to the spectroscopic measurement, the measurement of R_p based on the method described in ref. 22, by the use of a blackbody light source at 500°C , was conducted to observe the overall dependence on V_b and detector temperature. The radiation was incident on the detector through a chopper, and the photoconductive current was measured with a lock-in amplifier (SRS, SR830).

The reflection spectra were measured with an infrared microscope equipped with a Cassegrain objective lens connected to the FTIR. A relatively small incidence angle distribution centered at 26° was realized with an aperture.

Measurement of electrical properties. To measure the dark current, the detector was covered by a cold shield with a blackbody coating cooled at the same temperature as the detector (e.g., 78 K). When the cold shield is removed, a background light at 298 K is incident on the detector from an area with an effective FOV of 102° . The current-voltage relationship was measured with a source meter (Keithley, 2635B).

To determine the values of dark-current-limited detectivity and g , the power spectral density of the amplified current was measured with a fast Fourier transform analyzer (Ono Sokki, CF-4700). The value of g (Supplementary Fig. 2a) was determined from the dark current, I_{dark} , and noise spectral density $i_n/\Delta f^{1/2}$ (Δf : bandwidth) by the relationship $i_n/\Delta f^{1/2} = (4egI_{\text{dark}})^{1/2}$. The noise spectra exhibited a plateau-like region in the range of 0.5–3 kHz. In this study, the value at 1 kHz was used³⁴.

Data availability

The authors declare that the data supporting the findings of this study are available within the paper and its Supplementary information files.

Received: 27 November 2019; Accepted: 8 January 2020;

Published online: 28 January 2020

References

- Yagi, H. Beam transmission of ultra short waves. *Proc. IRE* **16**, 715–741 (1928).
- Kraus, J. D. & Marhefka, R. J. *Antennas for All Applications*. ed. 3, (McGraw Hill, New York, 2002).
- Kosako, T., Kadoya, Y. & Hofmann, H. F. Directional control of light by a nano-optical Yagi–Uda antenna. *Nat. Photon* **4**, 312–315 (2010).
- Yu, N. et al. Light propagation with phase discontinuities: generalized laws of reflection and refraction. *Science* **334**, 333–337 (2011).
- Kao, T.-Y., Reno, J. L. & Hu, Q. Phase-locked laser arrays through global antenna mutual coupling. *Nat. Photon* **10**, 541–546 (2016).
- Lévêque, G. & Martin, O. J. F. Tunable composite nanoparticle for plasmonics. *Opt. Lett.* **31**, 2750–2752 (2006).
- Liu, X., Starr, T., Starr, A. F. & Padilla, W. J. Infrared spatial and frequency selective metamaterial with near-unity absorbance. *Phys. Rev. Lett.* **104**, 207403 (2010).
- Puscasu, I. & Schaich, W. L. Narrow-band, tunable infrared emission from arrays of microstrip patches. *Appl. Phys. Lett.* **92**, 233102 (2008).
- Miyazaki, H. T. et al. Ultraviolet-nanoimprinted packaged metasurface thermal emitters for infrared CO₂ sensing. *Sci. Technol. Adv. Mater.* **16**, 035005 (2015).
- Miyazaki, H. T. & Kurokawa, Y. Squeezing visible light waves into a 3-nm-thick and 55-nm-long plasmon cavity. *Phys. Rev. Lett.* **96**, 097401 (2006).
- Chen, Y. N. et al. Antenna-coupled microcavities for enhanced infrared photo-detection. *Appl. Phys. Lett.* **104**, 031113 (2014).
- Palaferrri, D. et al. Room-temperature nine- μm -wavelength photodetectors and GHz-frequency heterodyne receivers. *Nature* **556**, 85–88 (2018).
- Prangma, J. C. et al. Electrically connected resonant optical antennas. *Nano Lett.* **12**, 3915–3919 (2012).
- Kern, J. et al. Electrically driven optical antennas. *Nat. Photon* **9**, 582–586 (2015).
- Binzoni, T. et al. Mapping human skeletal muscle perforator vessels using a quantum well infrared photodetector (QWIP) might explain the variability of NIRS and LDF measurements. *Phys. Med. Biol.* **49**, N165–N173 (2004).
- Sun, J. et al. Design and fabrication of resonator-quantum well infrared photodetector for SF₆ gas sensor application. *J. Micro/Nanolith. MEMS MOEMS* **16**, 034504 (2017).
- Goldberg, A., Uppal, P. N. & Winn, M. Detection of buried land mines using a dual-band LWIR/LWIR QWIP focal plane array. *Infrared Phys. Technol.* **44**, 427–437 (2003).
- Schwarz, B. et al. Monolithically integrated mid-infrared lab-on-a-chip using plasmonics and quantum cascade structures. *Nat. Commun.* **5**, 4085 (2014).
- Shaltout, A. M., Shalae, V. M. & Brongersma, M. L. Spatiotemporal light control with active metasurfaces. *Science* **364**, eaat3100 (2019).
- Zheludev, N. I. & Kivshar, Y. S. From metamaterials to metadevices. *Nat. Mater.* **11**, 917–924 (2012).
- Atwater, H. A. & Polman, A. Plasmonics for improved photovoltaic devices. *Nat. Mater.* **9**, 205–213 (2010).
- Levine, B. F. Quantum-well infrared photodetectors. *J. Appl. Phys.* **74**, R1–R81 (1993).
- Schneider, H. & Liu, H. C. *Quantum Well Infrared Photodetectors: Physics and Applications* (Springer, Berlin, 2007).
- Davies, J. H. *The Physics of Low-Dimensional Semiconductors: An Introduction*. (Cambridge Univ. Press, Cambridge, 1998).
- Li, Q. et al. High-polarization-discriminating infrared detection using a single quantum well sandwiched in plasmonic micro-cavity. *Sci. Rep.* **4**, 6332 (2014).
- Rogalski, A. Infrared detectors: status and trends. *Quant. Electron* **27**, 59–210 (2003).
- Bohren, C. F. & Huffman, D. R. *Absorption and Scattering of Light by Small Particles* (John Wiley & Sons, New York, 1983).
- Miyazaki, H. T. & Kurokawa, Y. How can a resonant nanogap enhance optical fields by many orders of magnitude? *IEEE J. Sel. Top. Quantum Electron.* **14**, 1565–1576 (2008).
- Palaferrri, D. et al. Ultra-subwavelength resonators for high temperature high performance quantum detectors. *New. J. Phys.* **18**, 113016 (2016).
- Mano, T. et al. Double-sided nonalloyed ohmic contacts to Si-doped GaAs for plasmoelectronic devices. *ACS Omega* **4**, 7300–7307 (2019).
- Vučković, J., Lončar, M. & Scherer, A. Surface plasmon enhanced light-emitting diode. *IEEE J. Quantum Electron.* **36**, 1131–1144 (2000).
- Unterrainer, K. et al. Quantum cascade lasers with double metal-semiconductor waveguide resonators. *Appl. Phys. Lett.* **80**, 3060–3062 (2002).
- Williams, B. S. et al. Terahertz quantum-cascade laser at $\lambda=100\ \mu\text{m}$ using metal waveguide for mode confinement. *Appl. Phys. Lett.* **83**, 2124–2126 (2003).
- Levine, B. F. et al. High sensitivity low dark current 10 μm GaAs quantum well infrared photodetectors. *Appl. Phys. Lett.* **56**, 851–853 (1990).
- Rosencher, E., Luc, F., Bois, Ph & Delaitre, S. Injection mechanism at contacts in a quantum-well intersubband infrared detector. *Appl. Phys. Lett.* **61**, 468–470 (1992).
- Bandara, K. M. S. V., Levine, B. F., Leibenguth, R. E. & Asom, M. T. Optical and transport properties of single quantum well infrared photodetectors. *J. Appl. Phys.* **74**, 1826–1831 (1993).
- Liu, H. C. et al. High absorption (>90%) quantum-well infrared photodetectors. *Appl. Phys. Lett.* **79**, 4237–4239 (2001).
- Dionne, J. A., Sweatlock, L. A., Atwater, H. A. & Polman, A. Plasmon slot waveguides: towards chip-scale propagation with subwavelength-scale localization. *Phys. Rev. B* **73**, 035407 (2006).
- Kurokawa, Y. & Miyazaki, H. T. Metal-insulator-metal plasmon nanocavities: analysis of optical properties. *Phys. Rev. B* **75**, 035411 (2007).
- Wu, W., Bonakdar, A. & Mohseni, H. Plasmonic enhanced quantum well infrared photodetector with high detectivity. *Appl. Phys. Lett.* **96**, 161107 (2010).
- Le Perche, J., Desieres, Y. & Espiau de Lamaestre, R. Plasmon-based photosensors comprising a very thin semiconducting region. *Appl. Phys. Lett.* **94**, 181104 (2009).
- Sugimoto, Y. et al. Low propagation loss of 0.76 dB/mm in GaAs-based single-line-defect two-dimensional photonic crystal slab waveguides up to 1 cm in length. *Opt. Express* **12**, 1090–1096 (2004).
- Snider, G. 1D Poisson/Schrödinger: A band diagram calculator [<http://www.nd.edu/~gsnider/>].
- Vurgaftman, I., Meyer, J. R. & Ram-Mohan, L. R. Band parameters for III–V compound semiconductors and their alloys. *J. Appl. Phys.* **89**, 5815–5875 (2001).
- Ordal, M. A. et al. Optical properties of Au, Ni, and Pb at submillimeter wavelengths. *Appl. Opt.* **26**, 744–752 (1987).
- Palik, E. D. *Handbook of Optical Constants of Solids*. (Academic Press, San Diego, 1985).
- Maier, S. A. *Plasmonics: Fundamentals and Applications* (Springer, New York, 2007).
- Williams, B., S. Kumar, S., Hu, Q. & Reno, J. L. Operation of terahertz quantum-cascade lasers at 164 K in pulsed mode and at 117 K in continuous-wave mode. *Opt. Express* **13**, 3331–3339 (2005).
- Clawson, A. R. Guide to references on III–V semiconductor chemical etching. *Mater. Sci. Eng. R. Rep.* **31**, 1–438 (2001).

Acknowledgements

The authors acknowledge helpful discussion with an anonymous company, Y. Sakuma, T. Noda, A. Ohtake, D. Tsuya, N. Ikeda, E. Watanabe, K. Miyano, M. F. Hainey, Jr., M. Iwanaga and K. Sakoda. This work was supported by JSPS KAKENHI Grant Numbers JP15H02011, JP17H01275, and JP19H00875, Iketani Science and Technology Foundation, the Center for Functional Sensor and Actuator, the National Institute for Materials Science (NIMS), and the NIMS Nanofabrication Platform in Nanotechnology Platform Project sponsored by the Ministry of Education, Culture, Sports, Science and Technology, Japan.

Author contributions

H.T.M. conceived and designed the research, designed the antennas, and carried out the measurements. T.M. designed and fabricated the quantum well structures. T.Ks. fabricated the antennas with help from H.O, K.W. and Y.S. T.Kw. supervised the theoretical works on quantum wells. A.S. and Y.A. supervised wafer bonding. H.M. and T.O. supervised the theoretical works on antennas. Y.J. performed numerical analysis with contribution from H.M. H.T.M. wrote the paper, and the rest of the authors reviewed the same.

Competing interests

H.T.M. is named as an inventor in Japanese patent application No. 2019-230505, applied by National Institute for Materials Science and filed on 20 December, 2019.

Additional information

Supplementary information is available for this paper at <https://doi.org/10.1038/s41467-020-14426-6>.

Correspondence and requests for materials should be addressed to H.T.M.

Peer review information *Nature Communications* thanks the anonymous reviewers for their contribution to the peer review of this work.

Reprints and permission information is available at <http://www.nature.com/reprints>

Publisher's note Springer Nature remains neutral with regard to jurisdictional claims in published maps and institutional affiliations.



Open Access This article is licensed under a Creative Commons Attribution 4.0 International License, which permits use, sharing, adaptation, distribution and reproduction in any medium or format, as long as you give appropriate credit to the original author(s) and the source, provide a link to the Creative Commons license, and indicate if changes were made. The images or other third party material in this article are included in the article's Creative Commons license, unless indicated otherwise in a credit line to the material. If material is not included in the article's Creative Commons license and your intended use is not permitted by statutory regulation or exceeds the permitted use, you will need to obtain permission directly from the copyright holder. To view a copy of this license, visit <http://creativecommons.org/licenses/by/4.0/>.

© The Author(s) 2020